2008

Robust-Adaptive Magnetic Bearing Control of Flexible Matrix Composite Rotorcraft Driveline

Hans August DeSmidt
University of Tennessee - Knoxville, hdesmidt@utk.edu

Kon-Well Wang
University of Michigan - Ann Arbor, kwwang@umich.edu

Edward Smith
The Pennsylvania State University, ecs5@engr.psu.edu

Recommended Citation

DeSmidt, H.A., Wang K.W. and Smith, E.C., "Robust-Adaptive Magnetic Bearing Control of Flexible Matrix Composite Rotorcraft Driveline," Journal of the American Helicopter Society, Vol. 53, No. 2, pp. 115-124., 2008.

Robust-Adaptive Magnetic Bearing Control of Flexible Matrix Composite Rotorcraft Driveline

Hans A. DeSmidt,
Assistant Professor of Aerospace Engineering,
The University of Tennessee
Knoxville, TN, 37996
Tel: 865-974-5259
Fax: 865-974-5274
Email: hdesmidt@utk.edu

K. W. Wang,
William E. Diefenderfer Chaired Professor in Mechanical Engineering
The Pennsylvania State University
University Park, PA, 16801
kwwang@psu.edu

and

E. C. Smith,
Professor of Aerospace Engineering
The Pennsylvania State University
University Park, PA, 16801

ABSTRACT

Recent studies demonstrate that a key advantage of Flexible Matrix Composite (FMC) shaft technology is the ability to accommodate misalignments without need for segmenting or flexible couplings as required by conventional alloy and graphite/epoxy composite shafts. While this is indeed a very promising technology for rotorcraft driveshafts, the high damping loss-factor and thermal stiffness and damping sensitivities of the urethane matrix, makes FMC shafting more prone to self-heating and whirl instabilities. Furthermore, the relatively low bending stiffness and critical speeds of FMC shafts makes imbalance vibration a significant challenge to supercritical operation. To address these issues and advance the state-of-the-art, this research explores Active

Magnetic Bearing (AMB) technology together with a robust-adaptive hybrid H_∞ feedback/Synchronous Adaptive Vibration Control law designed to ensure stable supercritical operation of a prototype FMC rotorcraft driveline. The effectiveness of the proposed new approach is demonstrated through analysis of a helicopter driveline testbed.

NOMENCLATURE

A_c, A_n, A_T	=	system matrices
A_{cl}, A_{ncl}, A_{Tcl}	=	closed-loop system matrices
A_{cs}	=	shaft cross-sectional area, m^2
A_p	=	AMB pole face area, m^2
B_c, B_d, B_p, B_u	=	input matrices
B_{dcl}, B_{ucl}	=	closed-loop input matrices
$\mathbf{C}$	=	damping matrix
C_c, C_q, C_y, C_z	=	output matrices
C_{ycl}, C_{zcl}	=	closed-loop output matrices
$C_{FB}(s)$	=	H_∞ feedback controller
D	=	Rayleigh dissipation function, N-m/sec
d	=	disturbance input
D_c	=	control feed-through matrix
d_s	=	shaft outer diameter, m
E, E_n	=	shaft elastic moduli, N/m^2
e_{cc}	=	shaft eccentricity, m
E_l, E_t, G_{lt}	=	FMC ply moduli, N/m^2
f_v, f_w	=	AMB electromagnetic actuation forces, N
$f_{\max}, f_{rms}$	=	Peak and maximum RMS AMB forces, N
$\mathbf{G}$	=	gyroscopic matrix
G, G_n	=	shaft shear moduli, N/m^2
$G(s)$	=	H_∞ controlled system
h_{back}, h_{gap}	=	AMB clearances, m
i	=	SAVC control update number
I	=	shaft cross-section moment of area, m^4
I_{bias}, I_{sat}	=	AMB bias and saturation currents, Amps
I_v, I_w	=	AMB control current inputs, Amps
j	=	imaginary number, $\sqrt{-1}$
J	=	SAVC objective function, m^2
J_{FB}, J_{FBAVC}	=	shaft vibration metrics, m
k_i	=	AMB force-current gain, N/Amp
k_x	=	AMB negative levitation stiffness, N/m
$\mathbf{K}$	=	structural stiffness matrix
$\mathbf{K_{AMB}}$	=	AMB stiffness matrix
$\mathbf{K_{rd}}$	=	shaft whirl matrix
$L_{AMBi} [i = 1\text{-}3]$	=	AMB axial location, m

L_{IMB}	=	imbalance axial location, m
L_s	=	shaft length, m
$\mathbf{M}$	=	mass matrix
m_s	=	shaft mass, kg
n_c, n_x	=	number of states
n_{conv}	=	convolution window length
n_d, n_u, n_y, n_z	=	number of inputs and outputs
n_l	=	number of FMC ply layers
n_{mode}	=	number of modes
N_c, N_p	=	number of AMB coil turns and poles
N_v, N_w	=	8-dof 2-node beam shape functions
p	=	uncertainty channel input
$P(s)$	=	AMB-FMC driveline plant
q	=	uncertainty channel output
$\mathbf{Q_{\text{AMB}}, Q_{\text{IMB}}}$	=	force input matrices
R	=	SAVC weighting matrix
t	=	time, sec
T	=	shaft temperature, °C
T_{ke}	=	system kinetic energy, N-m
t_l	=	FMC ply layer thickness, m
T_n	=	nominal shaft temperature, °C
t_s	=	shaft wall thickness, m
T_s	=	sampling period, sec
T_u	=	SAVC update period, sec
T_{yu}	=	synchronous transfer matrix
u, u_{FB}, u_{SAVC}	=	control inputs, Amp
U	=	SAVC input Fourier vector
v, w	=	shaft lateral deflections, m
w_{eff}	=	SAVC weighting, m^2/Amp
x	=	axial position coordinate, m
x_c, x_p, x_{cl}	=	state vectors
y, z	=	system outputs
Y	=	SAVC output Fourier vector
$\delta W_{\text{IMB}}, \delta W_{\text{AMB}}$	=	Imbalance and AMB force virtual work
δ_c	=	FMC shaft damping-temperature sensitivity
δ_k, δ_τ	=	FMC shaft stiffness-temperature sensitivities
δ_T	=	deviation temperature, °C
$\delta_{T\text{stab}}$	=	stability margin, °C
$\delta_{T\text{conv}}$	=	convergence margin, °C
$\delta_{T\text{max}}$	=	robustness margin, °C
Δ	=	uncertainty block matrix
ΔT	=	deviation temperature bound, °C
ϕ_{IMB}	=	imbalance phase angle, radians
γ	=	H_∞ loop gain
η	=	modal coordinate vector

$\eta_l, \eta_t, \eta_{tl}$	=	FMC ply loss factors
μ_0	=	free-space permeability, N/Amps^2
ν_{tl}	=	FMC ply Poisson's ratio
θ_1, θ_2	=	FMC fiber angles, degrees
ρ_s	=	shaft density, kg/m^3
ω_i	=	natural frequencies, rad/sec
Ω	=	shaft speed, rad/sec
ξ, ξ_n	=	FMC shaft loss factor
ζ_i	=	modal damping ratios
$\bar{\rho}[\ ]$	=	spectral radius
" · "	=	derivative with respect to time
" ′ "	=	derivative with respect to x
" ∗ "	=	complex conjugate

INTRODUCTION

Recently, a novel approach to the design of helicopter tailrotor driveshafts based on newly emerging urethane/graphite Flexible Matrix Composite (FMC) materials has been explored in Refs. 1-5. It has been found that shafts constructed of such FMC materials can provide many benefits over conventional alloy and graphite/epoxy driveshafts. In particular, Refs. 1 and 2 found that, through proper tailoring of the FMC ply thickness and fiber orientations, FMC driveshaft designs with high torsion stiffness and low bending stiffness can be achieved with less-weight than conventional alloy shaft designs. Due to the high strain capability of FMC materials (see Ref. 3), Refs. 1 and 2 showed that a single-piece (non-segmented) FMC shaft can safely accommodate tailrotor driveline angular misalignments and eliminate the need for flexible couplings, which are a significant source of driveline vibration and maintenance requirements (Refs. 6 and 7).

While FMC driveshaft technology is indeed promising for rotorcraft applications, there are still research issues to be addressed before the concept can be fully utilized. For example, FMC shafts have been found to have significantly more structural damping as compared with conventional alloy or graphite/epoxy shafts, (Ref. 3). Consequently, as shown in Refs. 1 and 2,

FMC shafts are more prone to rotating-frame damping-induced whirl instability when operated supercritically. In particular, Ref. 2 conducted a comprehensive FMC tailrotor driveshaft design study which considered misalignment capability, whirl stability and imbalance vibration response. Here, since large misalignment capability essentially requires lower bending stiffness and consequently lower bending natural frequencies (i.e. critical speeds), it was concluded that there is a trade-off between misalignment capability and stability. As a result, the FMC driveline designs tended to be supercritical, thus, requiring fixed-frame damping to prevent whirl instability, see Ref. 8.

The major cause of vibration in composite driveshaft systems is shaft imbalance which produces synchronous vibration at the shaft operating speed harmonic. In particular, Ref. 9 explored the balancing of composite driveshafts with imbalance produced by density variations distributed along the shaft. These density variations, which are attributed to the composite shaft manufacturing process, are inherently unknown. As a result of manufacturing tolerances and relatively low bending stiffness of FMC shaft designs, Refs. 1 and 2 found that imbalance vibration magnitudes tended to be higher as compared with conventional alloy drivelines. Thus, imbalance vibration suppression of composite shafts, and FMC shafts in particular, is especially challenging.

To address these issues and advance the state-of-the-art toward reducing driveline vibration and maintenance requirements, the objective of this investigation is to explore the use of actively controlled magnetic bearing technology in conjunction with recently developed FMC shaft designs. By replacing the conventional rolling contact hanger bearings with non-contact Active Magnetic Bearings (AMB), and replacing the multi-segment flexible-coupling/shaft arrangement

with a single-piece FMC design, this new actively controlled, AMB-FMC driveline configuration offers significant vibration reduction and maintenance saving potential.

Many researchers have investigated the use of AMBs for active feedback controlled vibration suppression in various shaft and driveline systems. In particular, Ref. 10 investigated the size, weight, and power requirements of an AMB control system under full-state feedback optimal control for a particular helicopter tailrotor driveline. Here, it was concluded that the use of AMBs would be feasible in a rotorcraft setting. Furthermore, Refs. 11 and 12 developed a slowly adapting Synchronous Adaptive Vibration Control (SAVC) technique for suppressing steady-state imbalance vibration in AMB/shaft systems. Recently, Ref. 13 developed a Multi-Harmonic Adaptive Vibration Control (MHAVC) scheme to address misalignment and load-torque induced multi-harmonic vibrations which arise in traditional segmented driveshafts connected by flexible couplings. The robustness of such control strategies to various types of uncertainties, such as operating condition and shaft stiffness variation, were explored in Refs. 13 and 14.

In the case of FMC shafts, Ref. 4, demonstrated that the FMC ply elastic moduli and damping loss-factors were temperature dependent. To account for this thermal sensitivity and ensure closed-loop robustness, this investigation develops a robust-adaptive vibration control strategy for the actively controlled AMB-FMC driveline system. This control law, based on a hybrid H_∞ Feedback/SAVC feed-forward approach, enables the FMC driveline concept by ensuring stable levitation and vibration suppression over a wide range of operating speeds, shaft temperature deviations, and imbalance uncertainties.

TECHNICAL APPROACH

AMB-FMC Driveline System

Figure 1 depicts the AMB-FMC driveline system investigated in this research. The system consists of a single piece FMC shaft, which is driven at constant rotational speed, Ω. The FMC shaft, with transverse deflections $v(x,t)$ and $w(x,t)$, is coupled to a fixed input-shaft and fixed output-shaft via rigid couplings and is supported by three non-contact, radial AMBs.
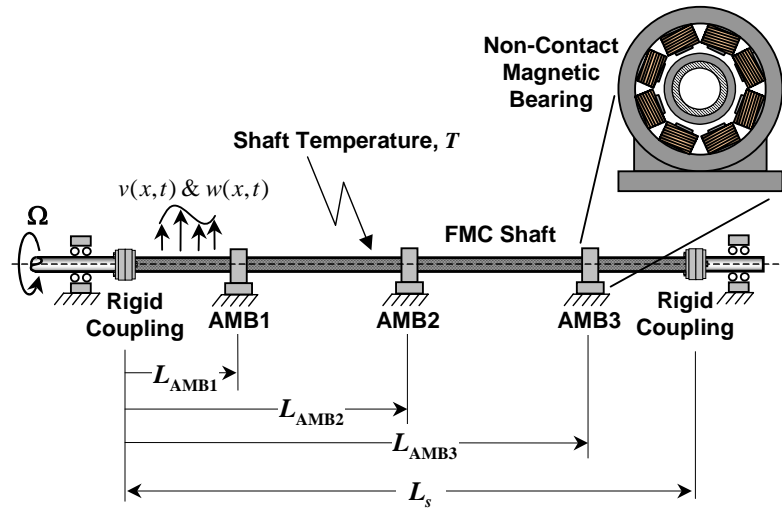
Fig. 1. AMB-FMC driveline system.

Furthermore, the shaft is composed of 8-ply layers which are assembled in a symmetric lay-up configuration. The ply orientations are described as $[+\theta_1/-\theta_1/-\theta_2/+\theta_2]_S$, where θ_1 and θ_2 are the fiber-orientation angles relative the shaft rotation axis. See Fig. 2.
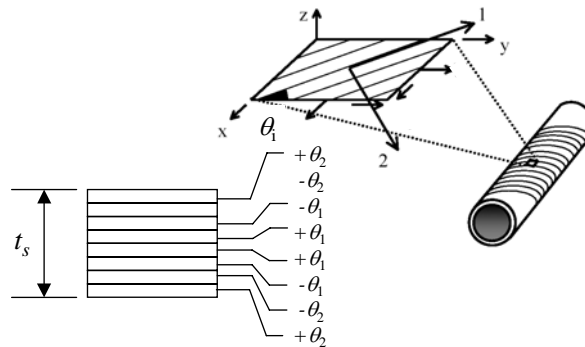
Fig. 2. Ply layer stacking sequence.

Based on θ_1 and θ_2 and the temperature dependent FMC ply material properties, the equivalent isotropic properties of the assembled FMC shaft are obtained via Equivalent Modulus Beam Theory (Ref. 15) and are represented as

$$E = E(T), \ G = G(T) \ \text{and} \ \xi = \xi(T) \tag{1-a}$$

Where E and G are shaft elastic and shear moduli, ξ is the equivalent viscous damping parameter and T is the shaft temperature. Also, the nominal shaft material properties are defined as

$$E_n = E(T_n), \ G_n = G(T_n) \ \text{and} \ \xi_n = \xi(T_n) \tag{1-b}$$

Where $T_n = 30°C$ is the nominal shaft temperature. Finally, the shaft material property temperature dependence is linearly approximated about the nominal values as (Ref. 4)

$$E(T) \approx (1 + \delta_T \delta_k) E_n, \ \ G(T) \approx (1 + \delta_T \delta_\tau) G_n$$
$$\xi(T) E(T) \approx (1 + \delta_T \delta_c) \xi_n E_n \tag{1-c}$$

Where δ_k, δ_τ, and δ_c, are bending stiffness, torsion stiffness and damping temperature sensitivities and $\delta_T = T - T_n$ is the deviation temperature about T_n due to some external ambient temperature operating condition. The material properties of the FMC shaft considered in this study are summarized in Tables 1 and 2.

Table 1 FMC Properties and Ply Configuration

FMC Ply Material Properties [a]	
Longitudinal modulus, E_l	115 GPa
Transverse modulus, E_t	0.275 GPa
Shear modulus, G_{lt}	0.250 GPa
Longitudinal loss-factor, η_l	0.0011
Transverse loss-factor, η_t	0.080
Shear loss-factor, η_{tl}	0.085
Poisson's ratio, ν_{tl}	0.38
FMC Shaft Ply Configuration	
Number of ply layers, n_l	8
Ply layer thickness, t_l	0.386 mm
Fiber orientations, θ_i	$[+45°/-45°/-90°/+90°]_s$

Table 2 Equivalent Isotropic Properties

FMC Shaft Equivalent Isotropic Properties	
Density, ρ_s	1650 kg/m³
Elastic modulus (nominal), E_n	11.84 GPa
Shear modulus (nominal), G_n	14.51 GPa
Equivalent viscous damping [a], ξ_n	5.85 x10⁻⁵
Temperature Sensitivity Parameters	
Bending stiffness sensitivity, δ_k	-0.1125 % / °C
Torsion stiffness sensitivity, δ_τ	-3.6x10⁻³ % / °C
Damping sensitivity, δ_c	0.225 % / °C

[a] Viscous damping based on loss-factor at 10 Hz

The system kinetic energy, T_{ke}, strain energy V, dissipation function, D, and virtual work expressions, δW_{IMB} and δW_{AMB}, due to shaft imbalance and the AMB control forces are

$$T_{ke} = \frac{\rho_s}{2} \int_0^{L_s} [A_{cs}(\dot{v}^2 + \dot{w}^2) + I(\dot{v}'^2 + \dot{w}'^2) + 2I(\Omega^2 + \Omega[w'\dot{v}' - v'\dot{w}'])]\,dx \qquad (2\text{-a})$$

$$V = \frac{EI}{2} \int_0^{L_s} [v''^2 + w''^2]\,dx \qquad (2\text{-b})$$

$$D = \xi \frac{EI}{2} \int_0^{L_s} [\dot{v}''^2 + \dot{w}''^2 + 2\Omega(\dot{v}''w'' - \dot{w}''v'') + \Omega^2(v''^2 + w''^2)]\,dx \qquad (2\text{-c})$$

$$\delta W_{\text{IMB}} = m_s e_{cc} \Omega^2 \big[\cos(\Omega t + \phi_{\text{IMB}})\delta v + \sin(\Omega t + \phi_{\text{IMB}})\delta w\big]_{x=L_{\text{IMB}}} \qquad (2\text{-d})$$

$$\delta W_{\text{AMB}} = \sum_{i=1}^{3} \big[f_v^{(i)}(t)\delta v + f_w^{(i)}(t)\delta w\big]_{x=L_{\text{AMB}i}} \qquad (2\text{-e})$$

Where " · " and " ′ " indicate differentiation with-respect-to time, t, and x respectively. Furthermore, $f_v^{(i)}$ and $f_w^{(i)}$, are the lateral components of the electromagnetic forces applied to the shaft by the AMBs, which are modeled based on linearized force-current-displacement relations about a constant bias current level, I_{bias} (cf. Ref. 13 or 16 for details).

$$\begin{bmatrix} f_v^{(i)} \\ f_w^{(i)} \end{bmatrix} = \begin{bmatrix} k_x & \\ & k_x \end{bmatrix} \begin{bmatrix} v \\ w \end{bmatrix}\Bigg|_{x=L_{\mathrm{AMB}i}} + \begin{bmatrix} k_i & \\ & k_i \end{bmatrix} \begin{bmatrix} I_v^{(i)} \\ I_w^{(i)} \end{bmatrix} \tag{3-a}$$

$$k_x = 4\cos\left(\frac{\pi}{8}\right)\mu_0 A_p N_c^2 \frac{I_{\mathrm{bias}}^2}{h_{\mathrm{gap}}^3} \quad \text{and} \quad k_i = 4\cos\left(\frac{\pi}{8}\right)\mu_0 A_p N_c^2 \frac{I_{\mathrm{bias}}}{h_{\mathrm{gap}}^2} \tag{3-b}$$

Here, $I_v^{(i)}$ and $I_w^{(i)}$, are the ith AMB control current inputs which are determined by the active control law. Based on Eqs. (2) and (3), the AMB-FMC driveline equations of motion are obtained via the Finite Element Method (FEM). For more details, one can refer to the Appendix. Finally, the model order is reduced via a modal transformation retaining the first $n_{\mathrm{mode}}=10$ modes. The resulting equations-of-motion in terms of modal coordinates, $\eta(t) \in \Re^{n_{\mathrm{mode}}\times 1}$, are

$$\begin{aligned} &\mathbf{M}\ddot{\eta} + \left[(1+\delta_T\delta_c)\mathbf{C} + \mathbf{G}(\Omega)\right]\dot{\eta} + \\ &\cdots \left[(1+\delta_T\delta_k)\mathbf{K} + (1+\delta_T\delta_c)\mathbf{K_{rd}}(\Omega) + \mathbf{K_{AMB}}\right]\eta \\ &\cdots = \mathbf{Q_{IMB}}\left[\sin\Omega t \quad \cos\Omega t\right]^T + \mathbf{Q_{AMB}}u(t) \end{aligned} \tag{4}$$

Where the matrices **M, C, G** and **K** are the nominal mass, structural damping, gyroscopic and elastic stiffness matrices, respectively, with **M = I** (identity matrix). **K_{rd}** is the skew-symmetric rotating-frame damping-stiffness matrix (Ref. 7) and **K_{AMB}**, is the negative AMB stiffness matrix for the bias current level I_{bias} (Ref. 13). Finally, $\mathbf{Q_{IMB}} \in \Re^{n_{\mathrm{mode}}\times 2}$ describes the shaft imbalance excitation and $\mathbf{Q_{AMB}} \in \Re^{n_{\mathrm{mode}}\times n_u}$ is the AMB force-current input distribution matrix with control current input vector $u(t) \in \Re^{n_u \times 1}$.

In this investigation, the proposed AMB-FMC driveline is sized to replace the conventional supercritical segmented tailrotor driveline of the McDonnell-Douglas AH-64 Apache helicopter. In particular, the overall driveline length, L_s, and shaft outer diameter, d_s, are kept the same as the original AH-64 driveline. Furthermore, the FMC shaft wall thickness, t_s, is selected such that the torsion stiffness of the new FMC driveline matches that of the original AH-64 driveline. The

parameters are summarized in Table 3. Finally the conventional hanger bearings and dampers are
replaced with the AMBs who's parameters are given in Table 4.

Table 3 Driveline Parameters

Shaft Dimensions	
Outer diameter, d_s	114.33 mm
Wall thickness, t_s	3.089 mm
Length, L_s	6.667 m
Shaft mass, m_s	11.88 kg
Cross-sectional area, A_{cs}	1079.63 mm^2
Moment of area, I	1.67x10^6 mm^4
Bearing Locations	
Location of AMB1, L_{AMB1}	1.33 m
Location of AMB2, L_{AMB2}	3.66 m
Location of AMB3, L_{AMB3}	5.34 m
Operating Conditions	
Operating speed, Ω	4815 RPM
Shaft eccentricity, e_{cc}	100 μm
Imbalance phase angle, ϕ_{IMB}	0°
Imbalance location, L_{IMB}	2.0 m

Table 4 Magnetic Bearing Parameters

AMB Parameters	
Rotor-stator airgap, h_{gap}	508 μm
Backup-bearing gap, h_{back}	225 μm
Bias current, I_{bias}	1.5 Amps
Saturation current, I_{sat}	3.0 Amps
Number poles, N_p	8
Pole face area, A_p	2.36 cm^2
Number of coil turns, N_c	168
Current stiffness, k_i	211.2 N/Amps
Position stiffness, k_x	623.45 N/mm
Peak force capacity, f_{max}	445 N
RMS force capacity, f_{rms}	311 N

To illustrate the effect of the FMC material thermal sensitivity on the driveline dynamic
characteristics, Fig. 3 shows the first five open-loop bending natural frequencies, ω_i, and modal
damping ratios, ζ_i, for a range of shaft temperatures.
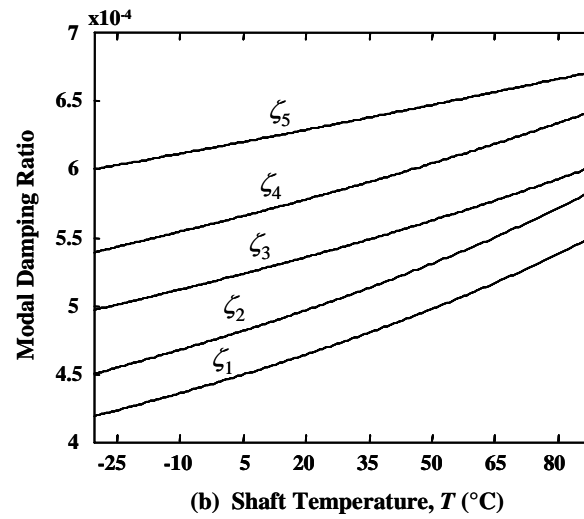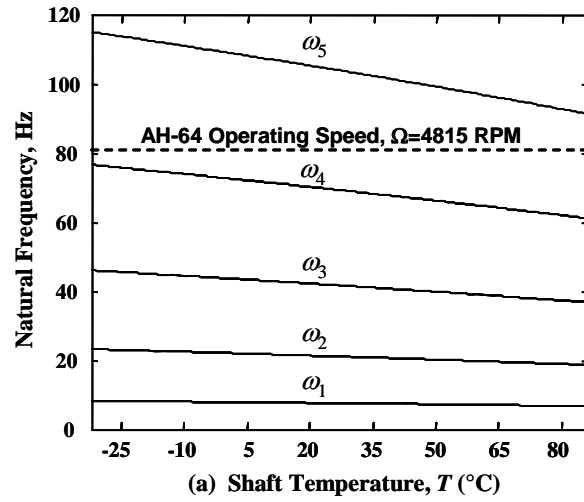
Fig. 3 FMC shaft dynamic characteristics vs temperature; (a) natural frequencies, (b) modal damping ratios.

Figure (3-a) demonstrates the high degree of lateral flexibly of the FMC driveline, where it is seen that the target operating speed is greater than the first four open-loop shaft natural frequencies.

Active Control Architecture

To proceed with the development of the active control law, the AMB-FMC driveline system in Eq. (4) is first recast into state-space form

$$\dot{x}_p = [A_n + \delta_T A_T] x_p + B_d d(t) + B_u u(t)$$
$$z = C_z x_p \tag{5}$$
$$y = C_y x_p$$

With state vector $x_p = [\eta^T \quad \dot{\eta}^T] \in \Re^{n_x \times 1}$ ($n_x = 20$), nominal system matrix, A_n, and deviation temperature-induced perturbation matrix, A_T.

$$A_n = \begin{bmatrix} 0 & I \\ -(K + K_{rd} + K_{AMB}) & -(C + G) \end{bmatrix}$$
$$A_T = \begin{bmatrix} 0 & 0 \\ -(\delta_k K + \delta_c K_{rd}) & -\delta_c C \end{bmatrix} \tag{6}$$

Also, $d(t) = [\sin \Omega t \cos \Omega t]^T$ is the synchronous disturbance input due to imbalance and $u \in \Re^{n_u \times 1}$ is the AMB control input with corresponding input distribution matrices $B_d \in \Re^{n_x \times n_d}$ and $B_u \in \Re^{n_x \times n_u}$ written as

$$B_d = \begin{bmatrix} 0 \\ Q_{IMB} \end{bmatrix} \text{ and } B_u = \begin{bmatrix} 0 \\ Q_{AMB} \end{bmatrix} \tag{7}$$

Additionally $y \in \Re^{n_y \times 1}$ and $z \in \Re^{n_z \times 1}$ are measured shaft displacement and performance output vectors respectively. Here, each AMB has two control axes and two displacement sensors, thus $n_u = n_y = 6$. Figure 4 is a block diagram of the closed-loop AMB-FMC driveline system.
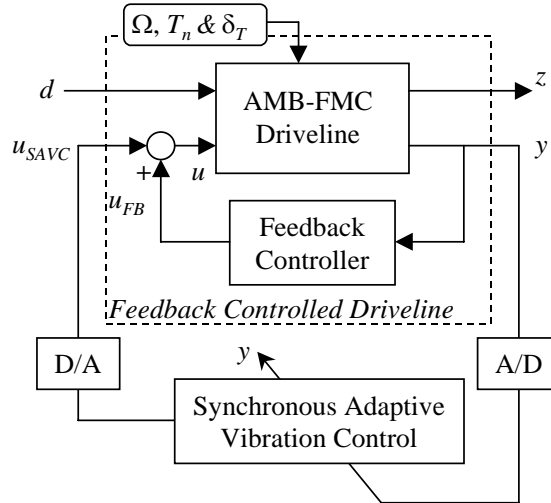
Fig. 4 Hybrid feedback/SAVC controlled AMB-FMC driveline system.

In this hybrid control strategy, the control input, u, consists of two components given in Eq. (8).

$$u(t) = u_{FB}(t) + u_{SAVC}(i,t) \tag{8}$$

Here, $u_{FB} \in \Re^{n_u \times 1}$ is generated from an output feedback control designed to stabilize the supercritical shaft whirl instabilities and to ensure bounded-input bounded-output (BIBO) stable levitation of the AMB-FMC driveline system in Eq. (5). Furthermore, the adaptive portion of the control, $u_{SAVC} \in \Re^{n_u \times 1}$, is

$$u_{SAVC}(i,t) = U_i(\sin \Omega t + j \cos \Omega t) \tag{9}$$

Where $U_i \in \Re^{n_u \times 1}$ is the ith updated complex Fourier coefficient control input which is adapted slowly relative to system transients to suppress the steady-state synchronous imbalance response.

In this investigation, the stabilizing portion of the control is synthesized based on a full-order dynamic output feedback controller, $C_{FB}(s)$, thus

$$C_{FB}(s) := \begin{cases} \dot{x}_c = A_c x_c + B_c y \\ u_{FB} = C_c x_c + D_c y \end{cases} \tag{10}$$

Where $x_c \in \Re^{n_c \times 1}$ is the controller state and $n_c = n_x$ is the controller order. From (5) and (10), the feedback controlled driveline system is

$$\begin{aligned} \dot{x}_{cl} &= A_{cl} x_{cl} + B_{dcl} d(t) + B_{ucl} u_{SAVC}(t) \\ z &= C_{zcl} x_{cl} \\ y &= C_{ycl} x_{cl} \end{aligned} \tag{11}$$

with augmented state vector $x_{cl} = [x_p^T \quad x_c^T]^T$ and

$$\begin{aligned} A_{cl} &= A_{ncl} + \delta_T A_{Tcl} \\ A_{ncl} &= \begin{bmatrix} A_n + B_u D_c C_y & B_u C_c \\ B_c C_y & A_c \end{bmatrix}, A_{Tcl} = \begin{bmatrix} A_T & 0 \\ 0 & 0 \end{bmatrix} \\ C_{ycl} &= [C_y \quad 0] \\ C_{zcl} &= [C_z \quad 0] \end{aligned}, \quad B_{dcl} = \begin{bmatrix} B_d \\ 0 \end{bmatrix}, \quad B_{ucl} = \begin{bmatrix} B_u \\ 0 \end{bmatrix} \tag{12}$$

Assuming the closed-loop feedback controlled AMB-FMC driveline system in Eq. (11) is BIBO stable, the Fourier coefficient vector, Y_i, of the measured steady-state response after the ith SAVC control input, U_i, is

$$Y_i = T_{yu} U_i + Y_{FB} \tag{13}$$

Where T_{yu} is the synchronous transfer matrix

$$T_{yu} = C_{ycl} \left[j\Omega I - A_{cl} \right]^{-1} B_{ucl} \tag{14}$$

and Y_{FB} is the steady-state imbalance response of the feedback controlled driveline without SAVC input (i.e. for $U_i = 0$).

The SAVC update law is obtained via least-squares minimization of the objective function J_i

$$J_i = Y_i^* Y_i + U_i^* R U_i \quad \text{with} \ R = w_{eff} I \tag{15}$$

where " $*$ " indicates complex conjugate transpose and w_{eff} (m^2/Amp), weights the SAVC control effort. Based on least-squares minimization of J_i, the SAVC update law is

$$U_{i+1} = [T_{yu}^* T_{yu} + R]^{-1} T_{yu}^* [T_{yu} U_i - Y_i] \tag{16}$$

Since the actual transfer matrix, T_{yu}, is a function the temperature uncertainty parameter, δ_T, the nominal transfer matrix at $T = T_n$

$$\hat{T}_{yu} = T_{yu} \Big|_{\delta_T = 0} = C_{ycl} \left[j\Omega I - A_{ncl} \right]^{-1} B_{ucl} \tag{17}$$

is utilized instead. Thus, the implemented SAVC update law is

$$U_{i+1} = [\hat{T}_{yu}^* \hat{T}_{yu} + R]^{-1} \hat{T}_{yu}^* [\hat{T}_{yu} U_i - Y_i] \tag{18}$$

Since the SAVC input is updated slowly relative to the settling-time of the feedback controlled driveline system in Eq. (11), the overall Hybrid feedback/SAVC controlled driveline is stable if and only if Eq. (11) is BIBO stable and if the SAVC adaptation process in Eq. (18) converges.

As detailed in Refs. 11 and 12, the SAVC input converges if and only if the following condition is satisfied.

$$\bar{\rho}\left[[\hat{T}_{yu}^{*}\hat{T}_{yu} + R]^{-1}\hat{T}_{yu}^{*}[\hat{T}_{yu} - T_{yu}]\right] < 1 \tag{19}$$

Where $\bar{\rho}[\ ]$ is the spectral radius with converged input and response, U_{SAVC} and Y_{FBAVC},

$$U_{SAVC} = -[\hat{T}_{yu}^{*}T_{yu} + R]^{-1}\hat{T}_{yu}^{*}Y_{FB}$$
$$Y_{FBAVC} = T_{yu}U_{SAVC} + Y_{FB} \tag{20}$$

In this investigation, errors between the actual T_{yu} and the estimated $\hat{T}_{yu}$ in the SAVC update law arise due to shaft temperature deviations δ_T about T_n. Since, according to (19), these errors could cause the SAVC not to converge, the convergence robustness with respect to δ_T must be considered in the control design.

Control Synthesis

Conceptually, in the hybrid feedback-SAVC control approach, the function of the feedback law in Eq. (10) is to ensure BIBO stable levitation of the AMB-driveline while the SAVC input adapts and converges to suppress the steady-state synchronous imbalance response. Since the slowly adapted SAVC input does not affect BIBO stability, the feedback controller and SAVC convergence designs can be conducted sequentially.

Because the control system must be robust with respect to temperature deviations about the nominal temperature, δ_T is considered as a bounded uncertainty parameter in the control design. Thus, the feedback/SAVC controlled AMB-FMC driveline system is rewritten as a linear fractional transformation (LFT) about the nominal feedback controlled system, $G(s)$, with deviation temperature uncertainty block $\Delta = \delta_T I$.
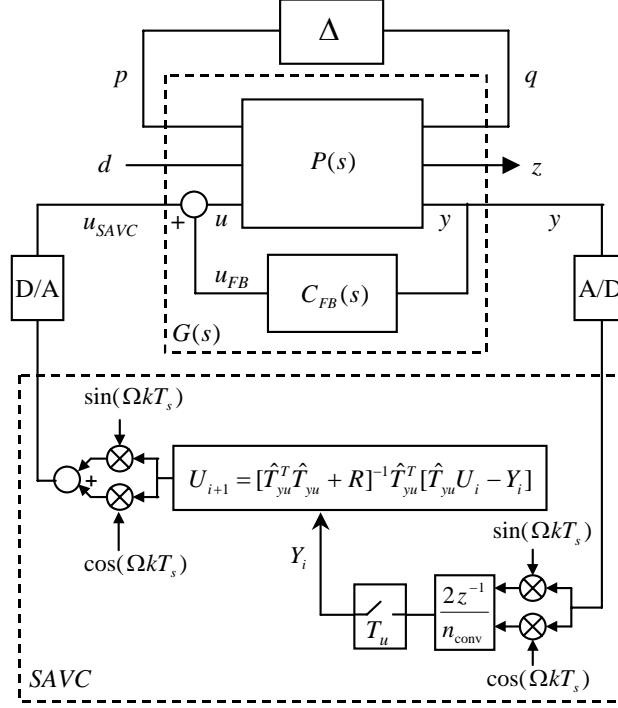
Fig. 5. Feedback/SAVC controlled AMB-FMC driveline with temperature uncertainty.

With nominal open-loop AMB-FMC driveline plant

$$P(s) := \begin{cases} \dot{x}_p = A_n x_p + B_p p(t) + B_d d(t) + B_u u(t) \\ q = C_q x_p \\ z = C_z x_p \\ y = C_y x_p \end{cases} \tag{21}$$

and with temperature dependent uncertainty matrix in Eq. (5) written as

$$\delta_T A_T = B_p \Delta C_q \text{ with } \Delta = \delta_T I \tag{22}$$

Where B_p and C_q describe the uncertainty structure.

To ensure that the feedback controlled closed-loop driveline system in Eq. (11) is robustly stable with respect to temperature deviations, δ_T, the feedback portion of the control, $C_{FB}(s)$, is synthesized using a robust H_∞ design approach.

In particular, $C_{FB}(s)$, is synthesized by minimizing the H_∞ norm of the closed-loop transfer function from $G_{qp}(s)$, over the set of stabilizing controllers (Ref. 17). Since $\|\Delta\|_\infty = |\delta_T|$, when

$\left\| G_{qp}(s) \right\|_\infty < \gamma$, BIBO stability of the feedback controlled driveline system is guaranteed for all bounded temperature deviations satisfying

$$|\delta_T| \le \delta_{T\text{stab}} = 1/\gamma \tag{23}$$

where $\delta_{T\text{stab}}$ is the deviation temperature robust stability margin. Here, based on the H_∞ analysis, there are no restrictions on the time variation $\delta_{T\text{stab}}$, only on the magnitude.

In this investigation, the H_∞ feedback controller is computed using the MATLAB® LMI Control Toolbox™ software package. For the AMB-FMC driveline system studied in this research, a feedback controller, $C_{FB}(s)$, which achieves $\gamma = 0.0034$ ($\delta_{T\text{stab}} = 163°C$) is synthesized. Since $\delta_{T\text{stab}} = 163°C$ is well above the expected shaft temperature deviations, this is considered a robust design and is utilized for the feedback portion of the hybrid feedback/SAVC law in the subsequent analysis.

To analyze the convergence robustness of the SAVC portion of the control, the convergence criteria in Eq. (19) is iteratively solved using a bisection algorithm to determine the deviation temperature robust convergence margin, $\delta_{T\text{conv}}$, for a range of shaft speeds. Finally, the overall deviation temperature robustness margin $\delta_{T\text{max}}$ for a given shaft speed, Ω, is defined and computed as

$$\delta_{T\text{max}} = \min[\delta_{T\text{stab}}, \, \delta_{T\text{conv}}] \tag{24}$$

To asses the vibration performance, the following worst-case steady-state vibration indices are defined for a given deviation temperature bound, ΔT

$$
\begin{aligned}
J_{FB}(\Delta T) &= \sup_{0 \le |\delta_T| \le \Delta T} \left[\frac{1}{n_y} \sqrt{Y_{FB}{}^* Y_{FB}} \right] \\
J_{FBAVC}(\Delta T, w_{eff}) &= \sup_{0 \le |\delta_T| \le \Delta T} \left[\frac{1}{n_y} \sqrt{Y_{FBAVC}{}^* Y_{FBAVC}} \right]
\end{aligned}
\tag{25}
$$

With $\Delta T \leq \delta_{T\max}$. Here J_{FB} and J_{FBAVC} measure the RMS imbalance vibration response of the driveline under H_∞ feedback and hybrid H_∞ feedback/SAVC control respectively.

CLOSED-LOOP PERFORMANCE

System at Nominal Temperature

In this section, the closed-loop performance of the H_∞/SAVC controlled AMB-FMC driveline at the nominal temperature, $T_n=30°C$, is investigated assuming no temperature deviations or uncertainty, i.e. $\delta_T=0$. In particular, Fig. 6 shows the RMS vibration and control currents of the AMB-FMC driveline under H_∞ and H_∞/SAVC control with two amounts of SAVC control effort penalty weighting w_{eff}. Here, the H_∞/SAVC achieves significant vibration suppression compared with the H_∞ baseline except near two shaft speeds, $\omega_{c1} \approx 2800$ and $\omega_{c2} \approx 5500$ RPM. As expected, the case with the lowest SAVC penalty weighting, w_{eff}, achieves the best vibration suppression. Near the operating speeds, ω_{c1} and ω_{c2}, the SAVC requires excessive currents to suppress the vibration and thus, due to AMB current saturation limitations, the imbalance vibration cannot effectively be reduced at these speeds. This phenomena is due to transmission zeros, introduced into the control path by the H_∞ feedback controller $C_{FB}(s)$. These closed-loop transmission zeros at ω_{c1} and ω_{c2} block the effect of the SAVC input for speeds near ω_{c1} and ω_{c2}.
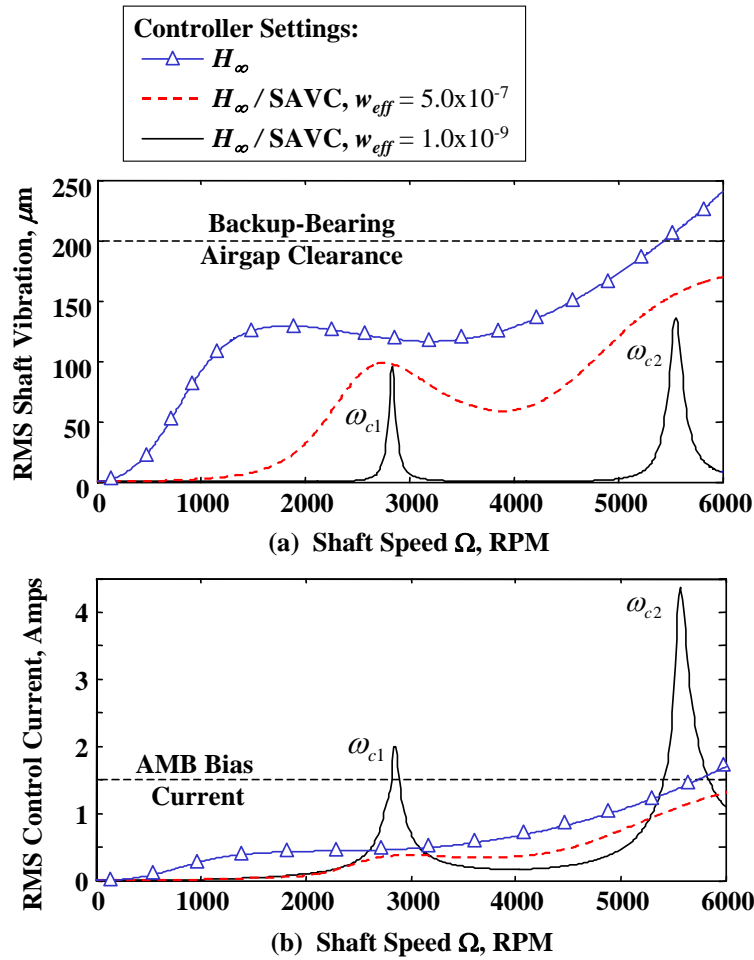
Fig. 6. RMS vibration and control currents vs. shaft speed for system at T_n=30°C.

However this blocking phenomena is not necessarily a serous issue, since most drivelines, such as helicopter drivelines, typically operate at a single, fixed speed, Ω. Thus, unless Ω corresponds with one of the transmission-zero speeds, the hybrid H_∞/SAVC law can be used to achieve effective vibration suppression. Nevertheless, one way to address this issue is through proper selection of the AMB locations along the driveline. It is found that the closed-loop transmission zeros speeds are very sensitive to the AMB locations, and thus they can be shifted away from a given operating speed by proper AMB placement. This sensitivity is demonstrated in Fig. 7, which shows the RMS vibration and control currents of the H_∞/SAVC controlled AMB-FMC driveline for two sets of AMB locations.
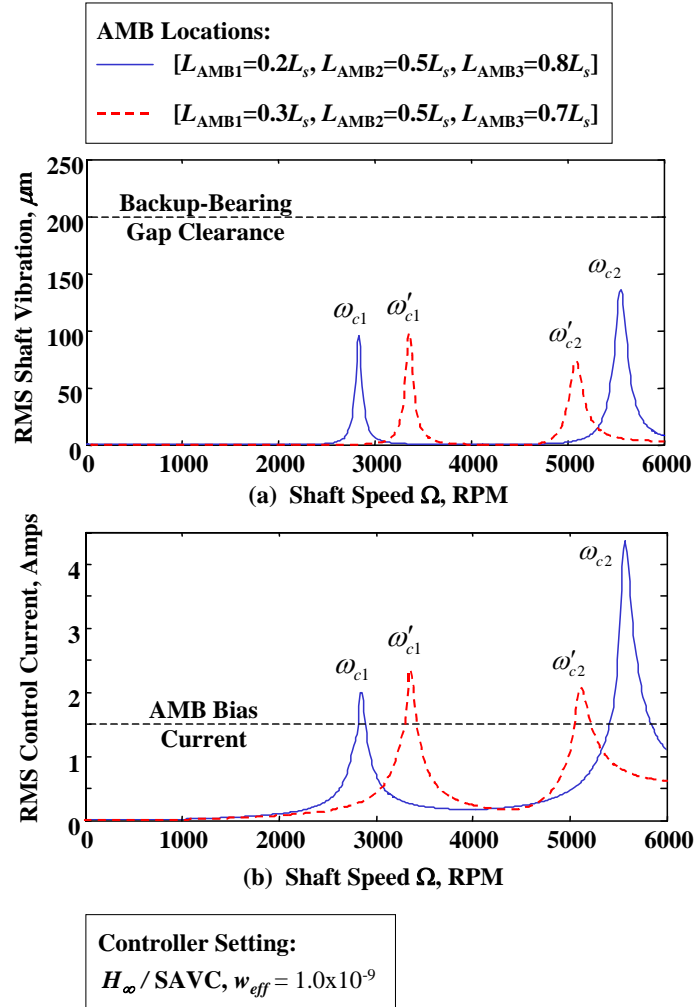
Fig. 7. Effect of AMB location on transmission-zero critical speeds.

System with Temperature Deviations

In this section the effect of temperature uncertainty, δ_T, is considered. Using Eqs. (24) and (25), the system robustness and imbalance vibration performance is analyzed over a range of shaft speeds, $\Omega = [0 - 6000]$ RPM. This speed range includes both sub and supercritical operation. Figure 8 shows how $\delta_{T\max}$ varies with Ω for several values of SAVC control effort penalty weighting, w_{eff}.
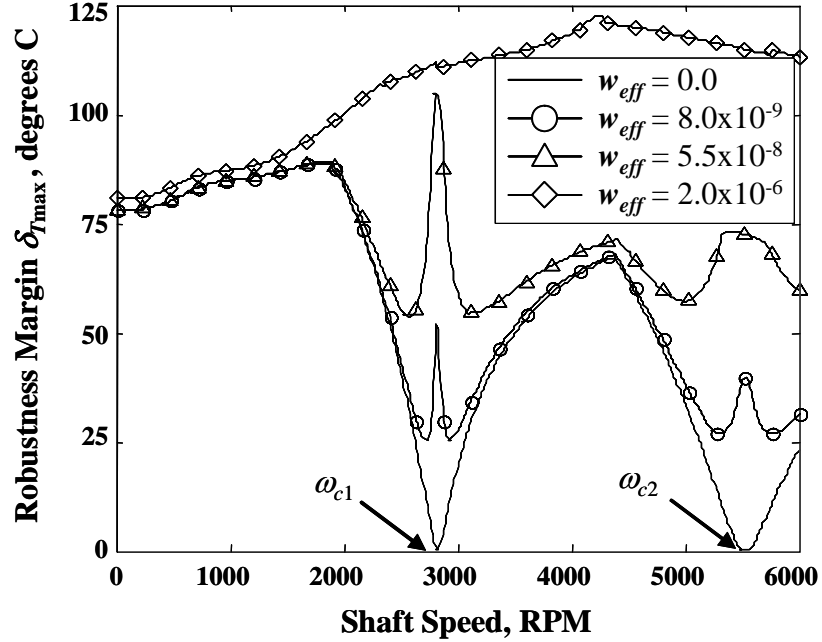
Fig. 8. Deviation temperature robustness margin vs. shaft speed for several values of SAVC control effort penalty weighting w_{eff} .

With no SAVC effort penalty (i.e. $w_{eff} = 0$), stability and convergence is guaranteed for temperature deviations of approximately $\pm 55°C$ about the nominal temperature, $T_n = 30°C$, over most of the RPM range. However, for operation near the closed-loop transmission-zero speeds ($\omega_{c1} \approx 2800$ and $\omega_{c2} \approx 5500$ RPM), the temperature robustness becomes significantly less. By penalizing the SAVC input (i.e. selecting $w_{eff} > 0$) the robustness margin near, ω_{c1} and ω_{c2}, can be increased significantly. In particular, as seen in Fig. 8 if w_{eff} is chosen to be $w_{eff} \geq w_{eff}^* = 5.5\text{x}10^{-8}$ m^2/Amp, the system can tolerate temperature deviations up to $\pm 55°C$ and still remain stable and converge across the entire operating RPM range. That is, $w_{eff} = w_{eff}^* = 5.5\text{x}10^{-8}$ m^2/Amp guarantees $\delta_{Tmax} > 55°C$ over the range $\Omega = [0 - 6000]$ RPM.

Considering $w_{eff} = w_{eff}^* = 5.5\text{x}10^{-8}$ m^2/Amp to be the lowest acceptable value for the design, the vibration performance for two values of $w_{eff} \geq w_{eff}^*$ is examined in Figs. 9 and 10. Here, the control system adapts and suppresses vibration without utilizing any knowledge of the shaft

imbalance or temperature deviation in the control synthesis. In each plot, the worst-case vibration performance indices, J_{FB} and J_{FBAVC}, are shown for both the nominal system and for a $\Delta T = 55°C$ deviation temperature uncertainty bound. By comparing the two performance indices, J_{FB} and J_{FBAVC}, and considering J_{FB} as the baseline performance, the effectiveness of the SAVC can be assessed.
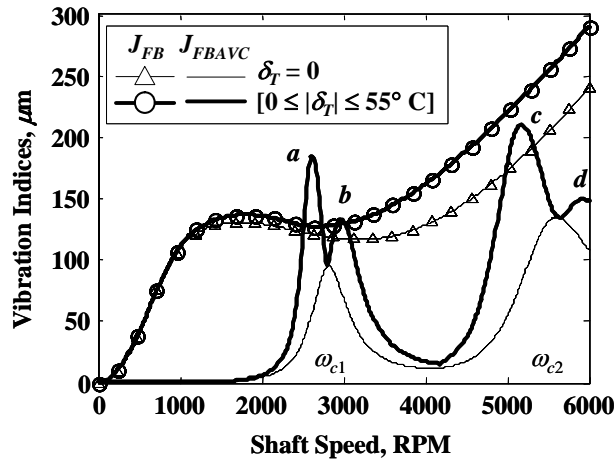
Fig. 9. J_{FB} **and** J_{FBAVC} **vs. shaft speed for deviation temperature uncertainty bounds; $[\delta_T = 0]$ and $[0 \le \delta_T \le 55°C]$, with $w_{eff} = 6.0 \times 10^{-8}$.**
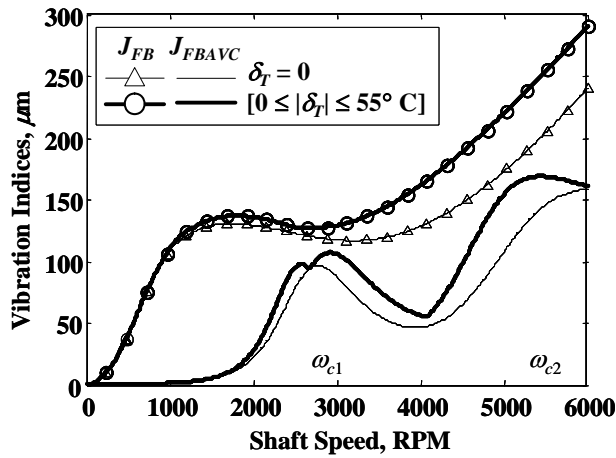
Fig. 10. J_{FB} **and** J_{FBAVC} **vs. shaft speed for deviation temperature uncertainty bounds; $[\delta_T = 0]$ and $[0 \le \delta_T \le 55°C]$, with $w_{eff} = 2.6 \times 10^{-7}$.**

Figure 9 demonstrates that, except for speeds near the closed-loop transmission-zero speeds, ω_{c1} and ω_{c2}, the SAVC successfully adapts and converges to achieve significant imbalance vibration

suppression even in the presence of temperature uncertainty δ_T. Thus, except for Ω near ω_{c1} and ω_{c2}, the hybrid H_∞/SAVC control law achieves robust performance. However, for speeds near ω_{c1} and ω_{c2}, the SAVC input is less effective, and the presence of the uncertainty, δ_T, causes the SAVC to increase the vibration above the feedback controlled baseline imbalance response, (see "a" and "b" in Fig. 9).

Since δ_T alters the FMC shaft stiffness and damping, δ_T also shifts the transmission-zero frequencies, ω_{c1} and ω_{c2} about their nominal values. This frequency shifting is reflected in the plots of the worst-case case performance indices by the presence of the peaks "a" and "b" about ω_{c1} and "d" and "c" about ω_{c2} in Fig. 9. The separation bandwidth between "a" and "b" and between "c" and "d" increases with the deviation temperature uncertainty δ_T.

Finally, comparing Figs. 9 and 10 demonstrates the effect of increasing w_{eff} on the SAVC vibration suppression performance and robustness. Increasing w_{eff} improves performance robustness for shaft speeds near ω_{c1} and ω_{c2}. However, it also limits the SAVC control input magnitudes which, in turn, reduces the maximum achievable vibration suppression. Therefore, larger values of w_{eff} are only necessary and beneficial for Ω near the closed-loop transmission-zero speeds, where the system is most sensitive to temperature uncertainty and a tradeoff between stability and vibration suppression must be made.

Time-Domain Response

This section explores the time-domain performance and robustness of the H_∞/SAVC controlled AMB-FMC driveline system subjected to shaft imbalance and temperature deviation δ_T. In the subsequent simulations, the A/D sampling period is $T_s = 1 \times 10^{-3}$ seconds, the SAVC control update period is $T_u = 1.0$ second, and the SAVC control effort weighting is $w_{eff} = 0$.

Furthermore, in each simulation, the system is initially operating under H_∞ feedback control until the SAVC portion is activated at $t = 4.0$ seconds. Figures 11 and 12 show the shaft response and AMB control current at speeds $\Omega = 3000$ RPM and $\Omega = 4815$ RPM for increasing shaft temperature deviation. According to Fig. 8, the deviation temperature robustness margin at these Ω corresponds to $\delta_{T\max} \approx 10°C$ and $\delta_{T\max} \approx 60°C$ respectively.
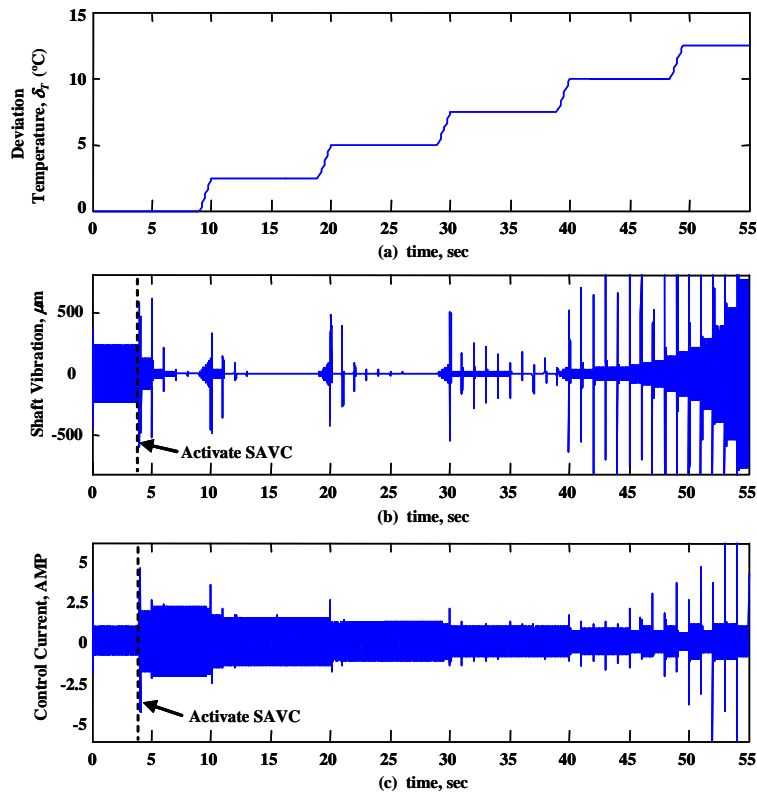
Fig. 11. H_∞/SAVC controlled AMB-FMC driveline response with $\Omega = 3000$ RPM and $w_{eff} = 0$; (a) deviation temperature, (b) shaft vibration, (c) AMB current.
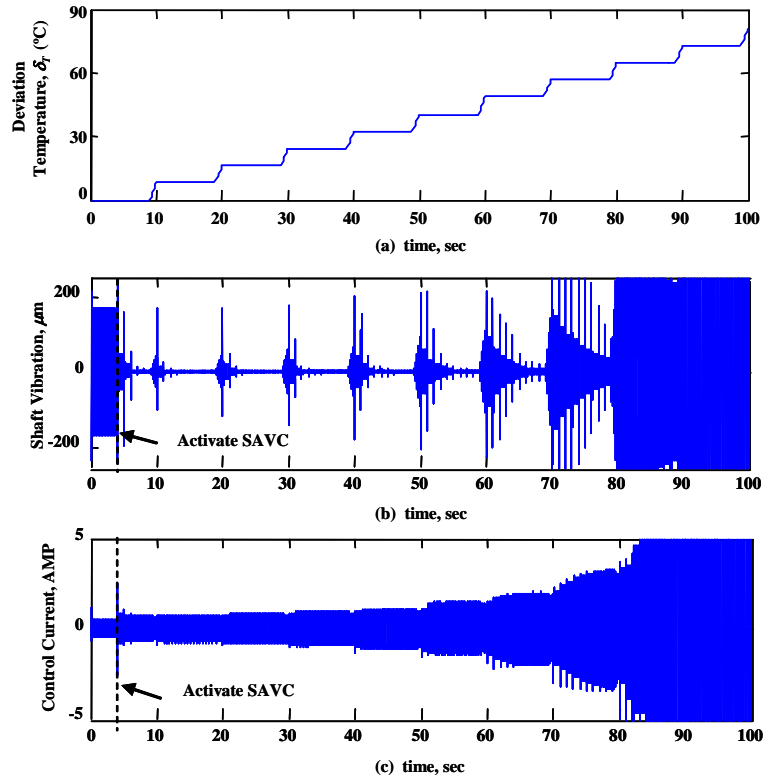
Fig. 12. *H∞*/SAVC controlled AMB-FMC driveline response with $\Omega = 4815$ RPM and $w_{eff} = 0$; (a) deviation temperature, (b) shaft vibration, (c) AMB current.

According to Figs. 11 and 12, the system is BIBO stable, and the adaptive control converges and effectively suppresses the imbalance vibration until $\delta_T > \delta_{T\max}$. These results numerically confirm the deviation temperature robustness margin predictions in Fig. 8.
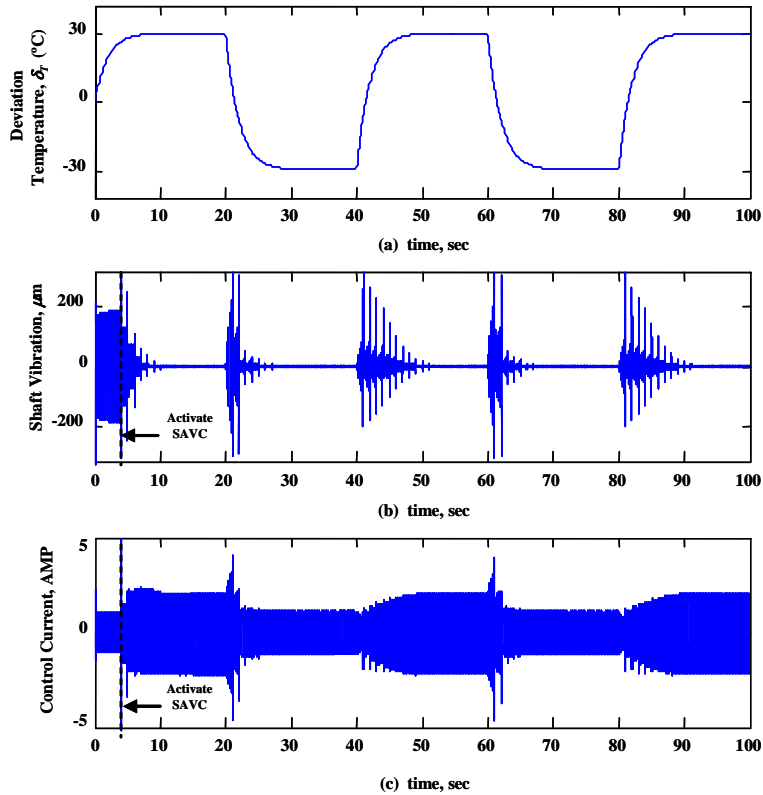
Fig. 13. H_∞/SAVC controlled AMB-FMC driveline response with $\Omega = 4815$ RPM and $w_{eff} = 0$; (a) deviation temperature, (b) shaft vibration, (c) AMB current.

Furthermore, Fig. 13 shows the system response for a cyclic deviation in shaft temperature. The simulation demonstrate that, for $\delta_T < \delta_{Tmax}$, the H_∞ feedback portion of the control maintains stable levitation at supercritical speeds while the SAVC input adapts and converges within a few update steps to effectively suppress the shaft vibration. Since this is achieved without utilizing any information about the imbalance or temperature deviation in the control algorithm, the H_∞/SAVC law developed in this research is deemed robust.

CONCLUSIONS

In this investigation, a hybrid H_∞ feedback/SAVC control law is developed for a prototype AMB-FMC tailrotor driveline system considering uncertainties due to temperature dependent FMC material properties, rotating-frame damping, and shaft imbalance. By proper selection of

the SAVC control effort parameter, w_{eff}, the hybrid H_∞/SAVC control strategy guarantees stable levitation and vibration suppression, and is robust with respect to FMC shaft temperature deviations and imbalance uncertainty. The resulting controller is effective across a wide range of sub- and supercritical operating speeds from $\Omega = [0 - 6000]$ RPM except near certain closed-loop transmission-zero speeds introduced by the H_∞ feedback portion of the control. For shaft rotational speeds away from the transmission-zero frequencies, the control system has inherent robustness. Consequently, both stability and effective imbalance vibration suppression (~95 % reduction) is guaranteed for a wide range of temperature deviations ($\pm$ 55°C about 30°C nominal). For shaft speeds near the closed-loop transmission-zeros, the closed-loop system is more sensitive to temperature deviations, however the robustness and vibration suppression near these speeds can be greatly improved by increasing the value of w_{eff}. Finally, it is determined that the transmission-zero frequencies are sensitive to the AMB locations and thus can be effectively shifted by proper AMB positioning to allow low vibration operation at any desired design operating speed. Through the combination of single piece, rigidly coupled, FMC driveshaft technology and non-contact magnetic bearings, the AMB-FMC driveline concept and associated robust adaptive control law developed in this investigation further advances the vision of low maintenance, low vibration technologies for rotorcraft drive systems.

APPENDIX

The FEM elemental matrices for the driveline system in Fig. 1 are

$$\mathbf{M}_{el}^i = \rho_s \int_0^{L_{el}^i} \left[A_{cs}(N_v^T N_v + N_w^T N_w) + I(N_v'^T N_v' + N_w'^T N_w') \right] dx \qquad \text{(A-1)}$$

$$\mathbf{C}_{el}^i = \xi EI \int_0^{L_{el}^i} (N_v''^T N_v'' + N_w''^T N_w'') dx \qquad \text{(A-2)}$$

$$\mathbf{G}_{el}^i = 2I\Omega \int_0^{L_{el}^i} (N_v'^T N_w' - N_w'^T N_v') \, dx \qquad \text{(A-3)}$$

$$\mathbf{K}_{el}^{i} = EI \int_{0}^{L_{el}^{i}} (N_v''^T N_v'' + N_w''^T N_w'') \, dx \qquad (A\text{-}4)$$

$$\mathbf{K}_{\mathbf{rd}el}^{i} = \xi \, EI\Omega \int_{0}^{L_{el}^{i}} (N_v''^T N_w'' - N_w''^T N_v'') \, dx \qquad (A\text{-}5)$$

ACKNOWLEDGMENTS

REFERENCES

[1] Mayrides, B., Smith, E. C., and Wang, K. W., "Analysis and Synthesis of Highly Flexible Helicopter Drivelines with Flexible Matrix Composite Shafting," Proceedings of the 61st American Helicopter Society Forum and Technology Display, Vol. 2, pp. 1582-1595, Grapevine, TX, June 1-3, 2005.

[2] Shin, E., Wang, K. W., and Smith, E. C., "Characterization of Flexible Matrix Composite Rotorcraft Driveshafts," Proceedings of the 59th American Helicopter Society Forum and Technology Display, 2003, Mesa, AZ.

[3] Shan, Y., and Bakis, C. E., "Static and Dynamic Characterization of a Flexible Matrix Composite Material," Proceedings of the 58th American Helicopter Society Forum and Technology Display, 11-13 June 2002, Montreal, Quebec.

[4] Shan, Y., and Bakis, C. E., "Frequency and Temperature Dependent Damping Behavior of Flexible Matrix Composite Tubes," 35th International SAMPE Technical Conference, September 28 -October 2, 2003, Dayton, OH.

[5] Shin, E., DeSmidt, H. A., Wang, K. W., and Smith, E. C., "Dynamic Characterization of Flexible Matrix Composite Driveshaft," *Proc. of the 13th International Congress on Sound and Vibration,* Vienna, Austria, July 2-6, 2006.

[6] Xu, M., and Marangoni, R. D., "Vibration Analysis of a Motor-Flexible Coupling-Rotor System Subjected to Misalignment and Unbalance. Part I: Theoretical Model and Analysis," *Journal of Sound and Vibration.,* 1994, pp. 663-679.

[7] Mazzei, A. J., Jr., Argento, A. and Scott, R. A., "Dynamic Stability of a Rotating Shaft Driven through a Universal Joint," *Journal of Sound and Vibration,* 1999, pp. 19-47.

[8] Zorzi, E. S. and Nelson, H. D., "Finite Element Simulation of Rotor-Bearing Systems with Internal Damping*," ASME Transactions, Journal of Engineering for Power*, 1977, pp. 71-76.

9. Darlow, M. S., Kraus, R. F. and Hetherington, P. L., "Demonstration of a Supercritical Composite Helicopter Power Transmission Shaft," Proceedings of The American Helicopter Society National Technical Specialist's Meeting on Advanced Rotorcraft Structures, Williamsburg, Va., October 25-27, 1988.

10. DeSmidt, H. A., Wang, K. W., and Smith, E. C., "Active Vibration Control of Rotorcraft Driveshaft-Airframe Dynamics," Proceedings of the 54th American Helicopter Society Forum and Technology Display, Washington, D. C., May 1998.

11. Knospe, C. R., Hope, R. W., Fedigan, S. J. and Williams, R. D., "Experiments in the Control of Unbalance Response using Magnetic Bearings," *Mechatronics,* 1995, pp. 385-400.

12. Knospe, C. R., Hope, R. W., Tamer, S. M. and Fedigan, S. J., "Robustness of Adaptive Unbalance Control of Rotors with Magnetic Bearings," *Journal of Vibration and Control*, 1996, pp. 33-52.

13. DeSmidt, H. A., Wang, K. W., and Smith, E. C., "Multi-Harmonic Adaptive Vibration Control of Misaligned Driveline via Magnetic Bearings: Theory and Experiment," Submitted to *Journal of Dynamic Systems, Measurement, and Control*, January 2006.

14. Knospe, C. R., Tamer, S. M. and Fedigan, S. J., "Robustness of Adaptive Rotor Vibration Control to Structured Uncertainty," *Journal of Dynamic Systems, Measurement, and Control*, 1997, pp. 243-250.

15. Jones, R. M., *Mechanics of Composite Materials*, McGraw-Hill, New York, 1975.

16. Humphris, R. R., Kelm, R. D., Lewis, D. W. and Allaire, P. E., 1986, "Effect of Control Algorithms on Magnetic Journal Bearing Properties," ASME Paper No. 86-GT-54.

17. Zhou, K., Doyle, J., and Glover, K., *Robust and Optimal Control,* Prentice-Hall, 1996.